

Shallow Cumulus Representation and Its Interaction with Radiation and Surface at the Convection Gray Zone

XABIER PEDRUZO-BAGAZGOITIA

Meteorology and Air Quality Group, Wageningen University and Research, Wageningen, Netherlands

PEDRO A. JIMÉNEZ

Research Applications Laboratory, NCAR, Boulder, Colorado

JIMY DUDHIA

Mesoscale and Microscale Meteorology Laboratory, NCAR, Boulder, Colorado

JORDI VILÀ-GUERAU DE ARELLANO

Meteorology and Air Quality Group, Wageningen University and Research, Wageningen, Netherlands

(Manuscript received 1 February 2019, in final form 24 April 2019)

ABSTRACT


This study presents a systematic analysis of convective parameterizations performance with interactive radiation, microphysics, and surface on an idealized day with shallow convection. To this end, we analyze a suite of mesoscale numerical experiments (i.e., with parameterized turbulence). In the first set, two different convection schemes represent shallow convection at a 9-km resolution. These experiments are then compared with model results omitting convective parameterizations at 9- and 3-km horizontal resolution (gray zone). Relevant in our approach is to compare the results against two simulations by different large-eddy simulation (LES) models. Results show that the mesoscale experiments, including the 3-km resolution, are unable to adequately represent the timing, intensity, height, and extension of the shallow cumulus field. The main differences with LES experiments are the following: a too late onset, too high cloud base, and a too early transport of moisture too high, overestimating the second cloud layer. Related to this, both convective parameterizations produce warm and dry biases of up to 2 K and 2 g kg^{-1} , respectively, in the cloud layer. This misrepresentation of the cloud dynamics leads to overestimated shortwave radiation variability, both spacewise and timewise. Domain-averaged shortwave radiation at the surface, however, compares satisfactorily with LES. The shortwave direct and diffuse partition is misrepresented by the convective parameterizations with an underestimation (overestimation) of diffuse (direct) radiation both locally and, by a relative 40% (10%), of the domain average.

1. Introduction

Shallow convective clouds disturb nonlinearly the coupling of several processes within the atmosphere (Arakawa 2004). The most relevant processes are the coupling between dynamics and radiation through light absorption, reflection and scattering by cloud droplets

(Liou 2002), the interaction between dynamic and microphysical processes by moisture and latent heat transport through the atmosphere (Grabowski 2014); and the surface–atmosphere coupling by altering the radiation budget at the surface (Trenberth et al. 2009) and subsequently creating dynamic heterogeneities (Gronemeier et al. 2016; Jakub and Mayer 2017).

Because of current limitations on simulating explicitly all the relevant scales and processes, convective parameterizations are used to represent the cloud dynamics. Similarly, the representations of radiation and surface processes need to be described in a parametric form. Convective parameterizations are developed

 Denotes content that is immediately available upon publication as open access.

Corresponding author: Xabier Pedruzo-Bagazgoitia, xabier.pedruzobagazgoitia@wur.nl

DOI: 10.1175/MWR-D-19-0030.1

© 2019 American Meteorological Society. For information regarding reuse of this content and general copyright information, consult the [AMS Copyright Policy \(www.ametsoc.org/PUBSReuseLicenses\)](https://www.ametsoc.org/PUBSReuseLicenses).

as stand-alone representations and are rarely tested in combination with other interactive processes. The works of [Lenderink et al. \(2004\)](#) and [Couvreur et al. \(2015\)](#) are representative studies of convective parameterizations on daily scales. However, none of them take into account possible radiative effects of the parameterized clouds on the atmosphere or at the surface. By prescribing radiative tendencies and surface fluxes, instead, they omit potential interactions and feedbacks relevant to the convection representation. Similarly, [Guichard et al. \(2004\)](#) did consider the effects of convection on radiation, but not the dynamic heterogeneities created at the surface.

Focusing first on turbulence-resolving large-eddy simulation (LES) in the scale of 50 m, previous studies have shown the relevance of the interaction between shallow cumulus (ShCu) and surface turbulent fluxes on diurnal scales: [Horn et al. \(2015\)](#) discussed how the explicit representation of cloud shading creates a larger population of shorter-lived and smaller clouds. In a series of systematic experiments with different assumptions on the surface representation, [Sikma et al. \(2018\)](#) found that spatially homogeneous noninteractive surface fluxes yield a cloud cover decrease of between 5% and 10% during the period of strongest convection. The coupling also influences the transport of moisture. It is reduced by more than 50% if cloud shading is neglected, and by up to 41% if the shading-related radiative effects are not treated locally ([Sikma and Vilà-Guerau de Arellano 2019](#)). [Jakub and Mayer \(2017\)](#) and [Klinger et al. \(2017\)](#) showed that cloud fields may have different morphology if the three-dimensional shortwave and longwave radiative effects, respectively, of clouds are included. All this evidence shows the need to include cloud-induced surface heterogeneities to investigate the impact on shallow convective parameterization studies.

Regarding models in which turbulence and moist convection are parameterized (i.e., mesoscale models), [Jimenez et al. \(2016a\)](#) studied the radiative effects of parameterized shallow convection at 9-km horizontal resolution using the mesoscale Weather Research and Forecasting (WRF) Model–Solar (WRF–Solar) ([Skamarock et al. 2008](#); [Jimenez et al. 2016b](#)). They used two mass-flux-type shallow convective parameterizations, namely those of [Deng et al. \(2003, 2014\)](#) and [Grell and Freitas \(2014\)](#). They found almost no seasonal bias from observations when the radiative effects at surface of both deep and shallow convection were taken into account for. Yet they did not study the cloud dynamics in the convective scheme.

Our aim is to extend on the previous studies to investigate the performance of convective parameterizations on a ShCu case with coupled radiation, turbulence,

and surface. To this end, we simulate a representative ShCu day with explicit coupling of the processes (i.e., LES), together with a process interaction represented by parameterized processes (i.e., mesoscale models). We pay special attention to key processes in the radiation–surface–cloud interactions. These are the following: first, the onset time, formation, intensity, and spatial characteristics of the cloud population; and second, the spatiotemporal variability of shortwave radiation, including direct and diffuse partitioning. This is key to plant transpiration and, consequently, to surface flux regulation.

The originality of our research strategy relies on a unique chain of numerical experiments of a representative ShCu field including coupled surface and radiative transfer schemes. By combining LES and mesoscale simulations we also investigate the performance of our experiments at (i) subgrid and (ii) terra incognita ([Wyngaard 2004](#); [Ching et al. 2014](#)). To support our analysis we make use of two LES models: DALES ([Heus et al. 2010](#)) and WRF–Solar in LES mode (hereafter, WRF–LES). The use of two different LES models ensures the consistency of our reference experiment. Our case is based on a typical late-summer day in the Netherlands over homogeneous grasslands, with an initially clear sky and shallow convection developing before noon ([Vilà-Guerau de Arellano et al. 2014](#); [Pedruzo-Bagazgoitia et al. 2017](#)). Keeping our experiments idealized and identical in initial and boundary conditions enables us to optimally control their performance.

[Section 2](#) describes the models and parameterizations as well as the design of the experiments. The main results of our work are displayed in [section 3](#), with DALES results present only in [section 3a](#). Our findings are discussed and placed in the context of literature in [section 4](#), where we also underline the relevance of our approach for related fields. The final comments and a summary of our findings are given in [section 5](#).

2. Methods

a. Simulating and representing

We perform two sorts of experiments in this study: experiments explicitly resolving most of the turbulent and cloud motions (i.e., LES experiments), and experiments with coarser resolution and parameterized turbulence, hereafter called mesoscale experiments. [Schalkwijk et al. \(2015\)](#) showed that mesoscale simulations do not resolve any of the (turbulent) motions below the time scale of hours and, thus, rely solely on the parameterizations. Meanwhile, LES resolves most

of the turbulence down to few minutes (Schalkwijk et al. 2015) (see Fig. 8 therein). Terminologically, we will refer to LES explicit experiments as simulations given that they explicitly resolve most of the motions and turbulent eddies within the domain following first principles. On the other hand, we will use terms representation or modeling when addressing results of mesoscale experiments.

b. WRF-Solar and the convective parameterizations

All the mesoscale experiments are performed using the mesoscale model WRF-Solar. It is based on the WRF Model (Skamarock et al. (2008)) with additional developments aimed at providing improved shortwave radiation-related information at surface (Jimenez et al. 2016b). Given the wide range of schemes and options in WRF-Solar, we will here focus briefly on the settings chosen for the present study. We use the Mellor–Yamada–Nakanishi–Niino (MYNN) scheme (Nakanishi and Niino 2006) to parameterize boundary layer turbulence in the mesoscale experiments. The microphysics scheme used is (Thompson et al. 2008), which considers cloud and rain drops, graupel, ice and snow in addition to water vapor. WRF-Solar computes the cloud fraction using a sum of liquid water and ice mixing ratios and dependent on the relative humidity at each grid box (Xu and Randall 1996; Hong et al. 1998). Information on radiative transfer and land surface model schemes is shown in section 2d.

Despite many schemes existing for deep convection, the parameterizations aiming at shallow convection are scarce. In our study we make use of two convective parameterizations: the one by Deng et al. (2014) was selected due to its original design addressed for shallow convection explicitly; the scheme by Grell and Freitas (2014) was selected because, although originally a deep convection scheme, there have been modifications to allow for shallow convection. In both parameterizations a smooth transition from shallow to deep convection is allowed.

The WRF parameterization for shallow convection by Deng et al. (2003, 2014) is a mass-flux-based parameterization also accounting for neutrally buoyant clouds (NBC). The triggering of the cloud is obtained by combining the explicitly resolved turbulent kinetic energy (TKE) and subgrid turbulence obtained from the boundary layer scheme (MYNN; Nakanishi and Niino 2006). The closure of this convection scheme transitions smoothly from a TKE closure on shallow convection, understood as updrafts up to 4 km, to a convective available potential energy closure in deeper convection similar to Kain and Fritsch (1990). In contrast to other convective parameterizations, it uses prognostic equations for subgrid cloud fraction, water and ice mixing ratios as

variables that are passed on to the radiation scheme. It provides a correction for cloud fraction dependent on the relative humidity of the gridbox cloud-free fraction. The reasoning is that computed cloud fraction is usually only linked to the size of the cloudy updraft, neglecting the radiative effect of NBCs detrained from the updrafts. The source term in the prognostic equations for subgrid cloud fraction, water and ice mixing ratios is a function of the rate of detrainment from the updrafts. The NBCs can dissipate through several physical processes, including evaporation at cloud edge due to horizontal turbulent mixing, vertical diffusion, precipitation, ice settling, and cloud-top entrainment instability. For a more in-depth description the reader is referred to Deng et al. (2003).

The other convective scheme used in this study is a mass-flux scale-aware stochastic convective parameterization (Grell and Freitas 2014). It is the latest version of a parameterization originally developed in Grell (1993) and extended by Grell and Devenyi (2002) with new modifications in the originating conditions of updrafts and downdrafts, trigger functions, inclusion of tracer transport and the possibility to allow for aerosol interactions. It diagnoses subgrid cloud ice and water content separately, but not subgrid cloud fraction. Thus, cloud fraction is computed following (Xu and Randall 1996; Hong et al. 1998) with the additional subgrid cloud and ice water content. The inclusion of Arakawa's approach (Arakawa et al. 2011) in the scheme ensures that the parameterization assumptions hold on the limits where the grid box is fully cloudy or fully clear. This parameterizations has been successful in representing a smooth transition of convection along scales at horizontal resolutions ranging from 5 to 20 km (Freitas et al. 2017), or from 3 to 50 km (Fowler et al. 2016). For a further insight in the parameterization, the reader is referred to Grell and Devenyi (2002) and Grell and Freitas (2014).

c. Explicit LES

We perform the explicit experiments with two LES models, WRF-LES and DALES. The Dutch Atmospheric Large Eddy Simulation (DALES; Heus et al. 2010; Ouwersloot et al. 2017) has its foundations in the work by Nieuwstadt and Brost (1986). The version used in this study is DALES 4.1 with improvements in the mechanistic vegetation submodel within the land surface scheme allowing for sensitivity to direct and diffuse shortwave radiation partition (Pedruzo-Bagazgoitia et al. 2017).

WRF-LES relies on the explicit mode of the WRF Model using the Smagorinsky closure (Smagorinsky 1963) as subgrid scheme. The advantage of using the WRF Model both for explicit as well as parameterized

TABLE 1. Overview and relevant settings of the numerical experiments in the study.

Experiment	Model	Domain ($X \times Y \times Z$) (km ³)	Gridpoint numbers	Time step (s)	Convective parameterization	Soil moisture (m ³ m ⁻³)	Soil temperature (top to bottom) (K)
DALES	DALES	24 × 24 × 5.5	480 × 480 × 456	Adaptive following CFL ^a	Explicit	0.385	282, 282.5, 283, 284
WRF-LES	WRF-Solar (LES mode)	24 × 24 × 20	480 × 480 × 200	0.3	Explicit	0.340	288, 288.5, 289, 290
WRF-LES_meso9	WRF-Solar (LES mode)	27 × 27 × 20	3 × 3 × 50	0.3	Explicit	0.340	288, 288.5, 289, 290
NOPAR_3	WRF-Solar	600 × 600 × 20	200 × 200 × 50	15	Explicit	0.340	288, 288.5, 289, 290
NOPAR_9	WRF-Solar	1800 × 1800 × 20	200 × 200 × 50	50	Explicit	0.340	288, 288.5, 289, 290
DENG_9	WRF-Solar	1800 × 1800 × 20	200 × 200 × 50	50	Deng et al. (2003)	0.340	288, 288.5, 289, 290
GF_9	WRF-Solar	1800 × 1800 × 20	200 × 200 × 50	50	Grell and Freitas (2014)	0.340	288, 288.5, 289, 290

^a Courant–Friedrichs–Lewy criterion: $CFL = \max(|u_i \Delta t / \Delta x_i|) = 1$ with Δt the time step in seconds and u_i and Δx_i the wind speed and grid spacing in meters and meters per second, respectively, in the direction i with $i = x, y, z$.

numerical experiments is that it allows us to discard discrepancies due to different model architectures.

The DALES and WRF-LES experiments present two main differences: the land surface model and the microphysics scheme. The former is described in section 2d. On the latter, DALES uses an all-or-nothing microphysics scheme with $q_l = q_{\text{tot}} - q_{\text{sat}}$ if $q_{\text{tot}} > q_{\text{sat}}$ and $q_l = 0$, otherwise, where q_l is the liquid water mixing ratio, q_{tot} the total water mixing ratio, and q_{sat} the saturation mixing ratio. DALES assumes a cloud fraction of 1 if $q_l > 0$ and 0 otherwise at each grid box. This scheme combination has been successfully used in previous studies (Siebesma et al. 2003; Vilà-Guerau de Arellano et al. 2014). WRF-LES uses the same new Thompson scheme and cloud fraction calculation method as WRF-Solar.

d. The coupled surface and radiative transfer schemes

All simulations make use of the RRTMG radiation scheme (Iacono et al. 2008). This scheme calculates the one-dimensional radiative fluxes for both longwave and shortwave, including direct and diffuse components, at every vertical level. The fluxes are calculated based on the local profiles of temperature, moisture and the standard profiles of the following compounds up to roughly 20 km: carbon dioxide, ozone, methane, nitrous oxide, oxygen, nitrogen, and the halocarbons. WRF and DALES present slightly different standard profiles, thus showing some disagreements in the radiation at the same height.

All the experiments in WRF-LES use the unified Noah land surface model (Niu et al. 2011) with four soil layers. The experiment in DALES uses an interactive land surface model responding to changing atmospheric conditions (van Heerwaarden et al. 2010) and includes the vegetation mechanistic model by Jacobs and de Bruin (1997) with further development on the vegetation sensitivity to direct and diffuse radiation (Pedruzo-Bagazgoitia et al. 2017). Differences

between surface schemes motivated different soil conditions in WRF-Solar or WRF-LES and DALES to obtain similar domain-averaged surface fluxes. Differences between surface schemes motivated different soil conditions in WRF and DALES to obtain similar domain-averaged surface fluxes on a clear day. The moisture and temperature of the four soil layers for each experiment are shown in Table 1.

e. Numerical setup and experiments

The case under study is inspired on an adaptation by Vilà-Guerau de Arellano et al. (2014) of late September observations in the Netherlands (Casso-Torralba et al. 2008). It shows an initially clear sky with shallow convection onset before noon and driven by the moisture and buoyancy at the surface. Highest cloud tops reach up to 4000 m. Our idealized study prescribes no large-scale forcings nor horizontal wind, and all simulations use bi-periodic boundary conditions.

All numerical experiments are performed between 0700 and 1700 UTC without spinup time. Regarding the latter, we prioritized the simultaneous start of all experiments at the expense of the experiment-dependent spinup time. The time stepping of each experiment is shown in Table 1.

We perform four mesoscale experiments, the first three differing in the convective parameterization used: no parameterization is used in NOPAR_9, the convective parameterization by (Deng et al. 2003) is used in DENG_9, and the GF_9 experiment uses the Grell–Freitas parameterization (Grell and Freitas 2014). The motivation for the NOPAR_9 experiment is twofold: to assess if explicit convection at 9-km horizontal resolution provides realistic results, and to discriminate between the effects of the boundary layer parameterization and the convective schemes. The grid spacing of these three mesoscale experiments is of 9 km in the horizontal, with 50 vertical levels

distributed along 20 km following typical mesoscale operational settings: the lowest level is 20 m thick, while at 5000 m high it is of about 400 m. The domain size for these simulations is of $1800 \times 1800 \text{ km}^2$. The last experiment, NOPAR_3, is identical to the NOPAR_9 experiment but with a 3 times finer grid spacing in the horizontal (i.e., 3 km). The domain size is of $600 \times 600 \text{ km}^2$. This experiment aims at showing whether the resolved convection at 3 km is enough to better represent the shallow convection compared to the parameterized DENG9, GF9, and the explicit NOPAR_9 experiments.

The WRF-LES and DALES experiments use a horizontal and vertical grid spacing of 50 and 12 m, respectively, with a domain of $24 \times 24 \text{ km}^2$. WRF-LES gradually stretches the vertical level thickness as it moves away from the surface, with a thickness of about 60 m at the maximum cloud top height at around 5000 m. The output of WRF-LES is averaged horizontally over 9 km and vertically in WRF-LES_meso9 to match the mesoscale experiments' grid resolution. The horizontal averaging included a double counting of about 15% of the grid points to obtain a domain of $27 \times 27 \text{ km}^2$. Thus the latter is not an experiment per se, but a regridding of an explicit experiment to determine the role of filtering small scales and to mimic the mesoscale resolution. We acknowledge the limited domain in WRF-LES_meso9 and assume that, although not statistically robust, a comparison with resolution-equivalent mesoscale simulations is insightful. We show DALES and WRF-LES experiments for the first part of the study to show the robustness of the case and the good agreement between different LES models. We keep only WRF-LES for the remaining part of the study to keep a as similar as possible model architecture between LES and mesoscale simulations. A brief overview on the experiments' settings and schemes is shown in Table 1.

3. Results

The development of ice–liquid water path (ILWP) over the whole domain is shown in Fig. 1. Both WRF-LES and DALES coincide on the onset of clouds happening at around 1100 UTC, with a linear growth until 1400 UTC and a further decrease starting after 1500 UTC. We define the shallow convection period as the time between 1100 and 1500 UTC. Between 1300 and 1500 UTC the ILWP stabilizes around 0.022 g m^{-2} with discrepancies between the two explicit LES simulations due to the chaotic behavior of shallow clouds and to the different microphysics schemes.

A lack of convective parameterizations delays the onset of clouds both at 9- and 3-km resolutions.

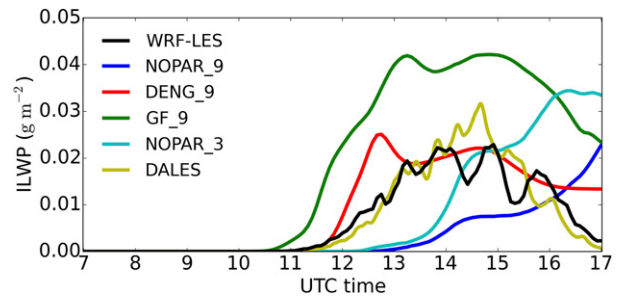


FIG. 1. Temporal evolution of the domain-averaged ice–liquid water path.

Furthermore, none of these two simulations predict a stabilization and decrease of ILWP. Instead, they show a delayed growth and a further increase even after 1500 UTC. The DENG_9 experiment shows an improvement in cloud onset time, and on the overall evolution of ILWP during the day, with a stabilization of ILWP at 1300 UTC and a (too little) decrease after 1500 UTC. However, it predicts a too fast growth of ILWP between 1200 and 1300 UTC. GF_9 predicts a too early onset of the first clouds by about 30 min, and, as with DENG_9, a too fast growth of ILWP during the early convection time reaching too high ILWP of up to 0.04 g m^{-2} .

The domain-averaged shortwave radiation (SW) at the surface (or global horizontal irradiance) and the normal direct and horizontal diffuse components are shown in Fig. 2. The first effects of clouds on global radiation appear at around 1130 UTC according to WRF-LES and DALES. The small differences between WRF-LES and DALES before this time are due to discrepancies in domain top heights and in the profiles of chemical compounds to which the radiation scheme RRTMG is sensitive, as mentioned in section 2.

GF_9 shows a decrease already by 1100 UTC while DENG gives a better timing for the first effect of clouds, consistent with Fig. 1. Afterward, diffuse radiation peaks at 100 W m^{-2} at around 1300 UTC while direct and global irradiance decrease due to cloud shading. After 1300 UTC the agreement between WRF experiments in global radiation is better, with underestimations of up to 8%, until the end of the shallow convection period. Due to the large ILWP overestimation by GF_9 shown in Fig. 1, this experiment underestimates the global radiation at the surface during the shallow convection period, especially in the 1100–1200 UTC period. There are important differences in the direct and diffuse contributions: only DALES and WRF-LES experiments predict a significant contribution of diffuse radiation at the surface ($\approx 100 \text{ W m}^{-2}$). The reason for this may be the large

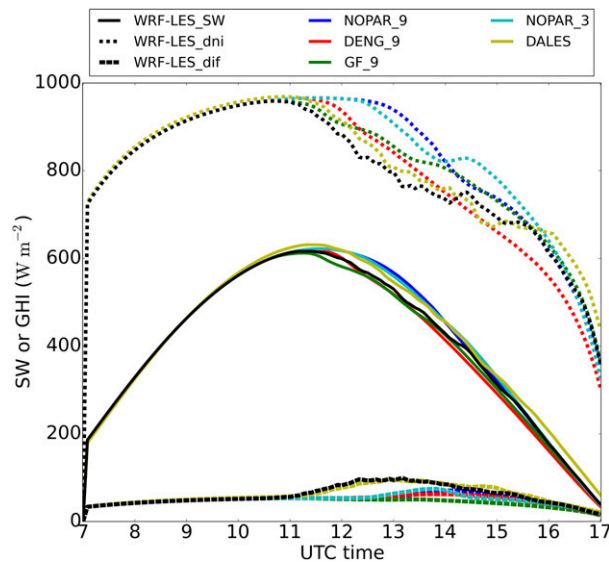


FIG. 2. Downward global horizontal (full), direct normal (dotted), and diffuse (dashed) irradiance at the surface for the three WRF mesoscale experiments, WRF-LES, and DALES.

nonlinearities between cloud depth and diffuse radiation, especially for very shallow clouds that cannot be resolved at a mesoscale resolution.

a. Thermodynamic characterization

Closely connected with the amount of available energy at the surface, we further explore the evolution of the atmospheric boundary layer (ABL) and cloud layer by showing the ice–liquid water potential temperature, θ_{il} , and total specific humidity, q_{tot} , in Figs. 3 and 4, respectively. The horizontal spatial variability within the domain is negligible in Fig. 3 and given by error bars at selected heights in Fig. 4. The results by DALES and WRF-LES experiments are consistent at all heights, with small discrepancies in boundary layer height and mixed-layer values for θ_{il} and q_{tot} of less than 0.2 K and 0.1 g kg^{-1} , respectively, due to differences in surface fluxes during the morning. The θ_{il} profiles of mesoscale experiments agree in the subcloud layer during the entire numerical experiment, and only until the cloud onset on layers above (not shown). There is a large spread among experiments, larger than within-experiment horizontal variability, in the moisture profiles below the cloud layer, indicating too little mixing in the boundary layer. This is also found in θ_{il} , although is less visible in Fig. 3. This finding is reinforced due to Bowen ratios of all WRF experiments differing by less than 5% (not shown). Such lack of mixing in the ABL is common in the MYNN scheme and leads to the underestimation of entrainment. Before cloud onset all mesoscale simulations underestimate (overestimate) turbulent kinetic

energy (TKE) in the upper (lower) half of the boundary layer by as much as 50% (not shown). NOPAR_3 improves the TKE representation within the ABL since the largest scales of TKE are now partly resolved (not shown). This improvement leads to a reduced entrainment underestimation on the mesoscale experiments, and consequently a reduction of the dry bias in the lower part of the cloud layer (not shown).

The atmosphere between 2000 and 5000 m shows a small but gradual cooling and moistening along the day in all experiments except for DENG_9 (Figs. 3 and 4). The moistening is a consequence of the rising moist updrafts. As a consequence of the observed underestimation in the boundary layer mixing, a drier layer above 1500 m and beyond intraexperiment variability is formed in the mesoscale experiments, being less severe in NOPAR_3. The cooling is driven by the longwave divergence caused by the water vapor gradient at that height (Fig. 4). The discrepancies in the magnitude of the cooling are partially explained by the effects of resolution (gray line in Fig. 3d at 3900 m). Our reasoning is that at higher vertical resolution there is a sharper gradient in water vapor that, in turn, creates a more localized cooling than that of the mesoscale experiments with a smoothed gradient due to reduced vertical levels. The reduced cooling in GF_9 is due to higher moisture content at higher elevations, thus weakening the sharp initial gradient and leading to a lower impact of longwave flux divergence. The DENG_9 experiment particularly overestimates the ice–liquid water potential temperature between 2000 and 5000 m after 1300 UTC, showing a 2-K warm bias at 3500 m by the end of the shallow convection period (1500 UTC). This is partly due to the significant presence of moisture as high as 6000 m already at 1330 UTC (Fig. 4b). Such high moisture content favors the early appearance of high clouds (Fig. 5a), which in turn causes the cooling by longwave divergence to happen at higher altitudes (almost 6000 m). Moisture profiles of such a shape were already schematically described by Lenderink et al. (2004) as typical of schemes overestimating mass flux. These features can also be related to an underestimation on the entrainment inside the updrafts by DENG_9, as it will be shown in Fig. 7. Related to this, DENG_9 showed too large cloud updraft velocities after 1200 UTC (not shown), which we hypothesize to be due to nonhydrostatic “pumping” (Deng et al. 2014). It is worth mentioning the accumulation of moisture after 1500 UTC, clearer for explicit simulations at around 3900 m (Figs. 4c,d), due to the moist and buoyant updrafts from the surface reaching the more stable layer above this height (Fig. 3). This moisture accumulation is key in the growth of a second cloud layer at around that height.

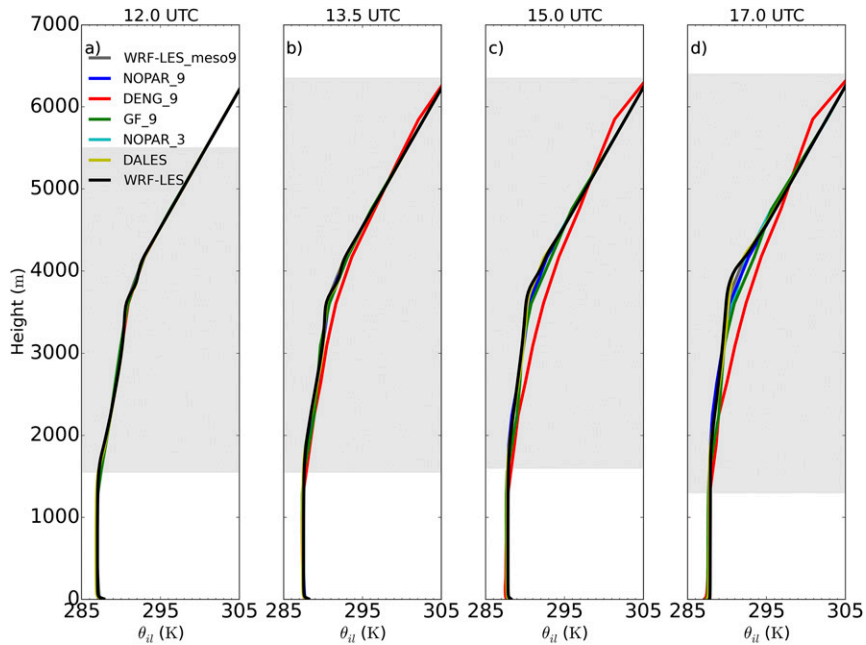


FIG. 3. Vertical profiles of domain-averaged ice-liquid water potential temperature θ_{ii} for the WRF mesoscale experiments, WRF-LES, DALES, and WRF-LES_meso9 at four times along the numerical experiment. The gray shades show the cloudy region in at least one of the experiments.

Results of the cloud fraction vertical profile averaged over the whole domain are presented in Fig. 5 at three stages during the shallow convection period. They corroborate the DENG scheme leading to the formation of

two cloud layers. Moreover, and comparing with WRF-LES, we find that simulations at 9-km horizontal resolution are unable to represent the vertical growth of the cloud layer, regardless of whether clouds are parameterized or

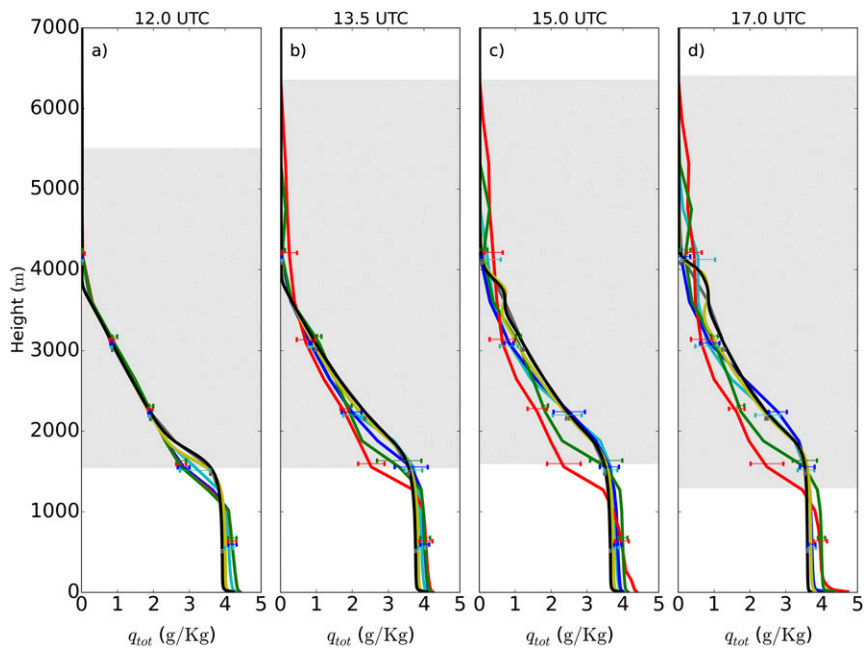


FIG. 4. As in Fig. 3, but for total water mixing ratio. Horizontal bars show the spatial standard deviation at selected heights for each experiment.

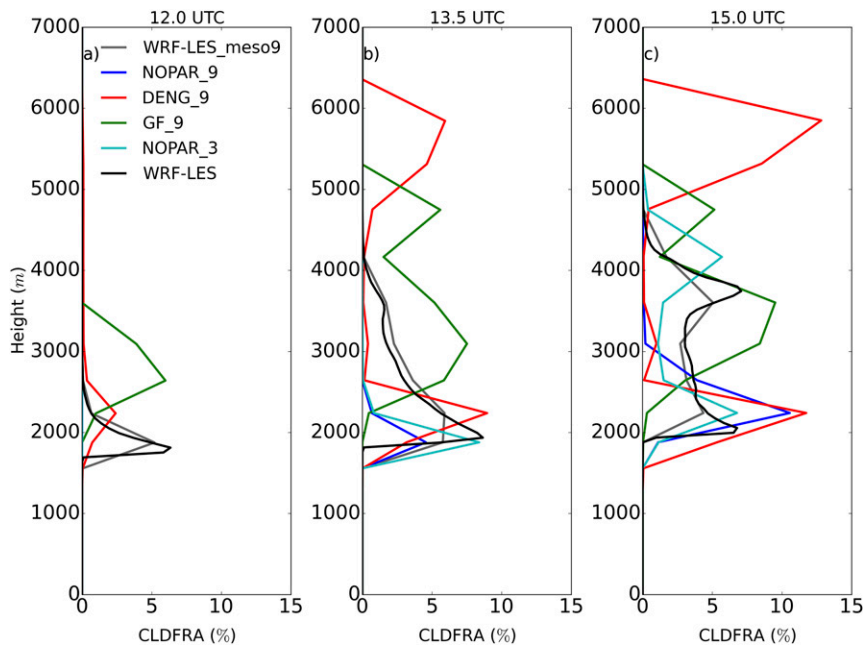


FIG. 5. Vertical profiles of domain-averaged cloud fraction at three times during the numerical experiment.

only resolved at mesoscale grid resolution. In particular, DENG_9 and GF_9 overestimate the superior cloud layer height and its growth rate (see Figs. 5b,c above 4000 m), while NOPAR_9 underrepresents and delays the vertical development of clouds. All mesoscale experiments show too much horizontal variability in cloud fraction, suggesting a nonhomogeneously distributed cloud fraction along the domain (not shown). The delay in cloud onset in NOPAR_9 is explained by the need of complete saturation in a $9 \times 9 \text{ km}^2$ grid box. We also observe that a fine vertical resolution is necessary to obtain a realistic time variability of cloud fraction. While in the LES experiments the cloud fraction varies in magnitude along the day (between 5% and 15% at 4000 m in from 1500 to 1600 UTC, not shown), the experiments with mesoscale resolution, including WRF-LES_meso9, are characterized by a much more constant cloud fraction vertical profile. Refining the horizontal resolution to 3 km without convection scheme (NOPAR_3) improves the cloud fraction profiles significantly, as it does capture the magnitude, although not the depth, of the shallow convection at 1330 UTC (Fig. 5b) and the two cloud layers at 1500 UTC. Yet the overestimation in the horizontal variability of cloud fraction by NOPAR_9 remains in NOPAR_3 (not shown).

b. Cloud field evolution

Focusing further on the cloud characteristics, a time series of mean and most frequent cloud base and cloud

top is shown in Fig. 6. The first noticeable feature is the spurious clouds created by GF_9 in the first moments of the experiment. This, however, is not relevant in the development of the numerical experiment as it happens in a very reduced area (Fig. 6e). The sporadic presence of precipitation after 1200 UTC may occasionally distort the cloud base calculations.

According to both of our LES experiments, first clouds appear at 1000 UTC at around 1700 m high. The base of most of the clouds follows the steady growth of the boundary layer along the day until about 1600 UTC, when we observe a jump in the height of the most common cloud base up to about 3500 m (Fig. 6c). This height represents the second cloud layer previously visible in Fig. 5c. However, we deduce from the ascending mean cloud base (Fig. 6a) that after 1300 UTC there is already a significant number of clouds starting above 2000 m high. We infer from the cloud top statistical mode that clouds remain very shallow until around 1330 UTC. At that point, the more buoyant surface layer combined with the more moist environment due to previous updrafts enhances the growth of clouds up to 4000 m. The continued longwave cooling and the increased moisture at those heights increases the persistence of clouds at 4000 m, as suggested by the rising mean cloud top and the jump in cloud top mode between 1300 and 1430 UTC.

The mesoscale experiment GF_9 represents correctly the onset of the first clouds, although, as pointed out in

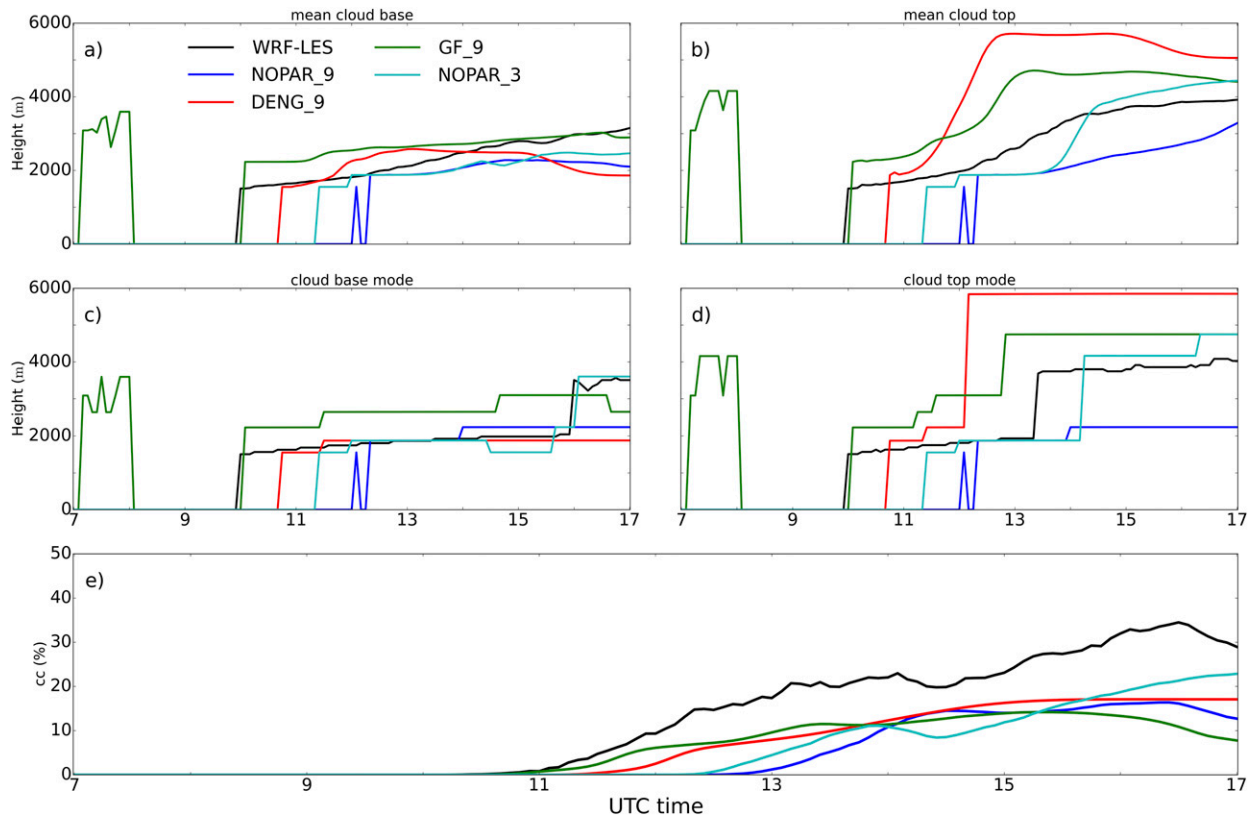


FIG. 6. Temporal series of (a) mean cloud base, (b) mean cloud top, (c) most frequent cloud base, (d) most frequent cloud top, and (e) cloud cover. The latter was calculated as the domain average of the column-integrated cloud fraction assuming maximum overlap.

Fig. 5a, it overestimates their height by at least 500 m. This height overestimation is due to the convective parameterization, as NOPAR_9 and DENG_9 give a better approximation to the initial cloud base and top heights. These two, however, miss the timing of the onset by almost 1 h. Figures 6b and 6d agree with the performance of DENG_9 shown in Figs. 4 and 5: that an initial overestimation in moisture transport leads to an early and too high cloud layer that remains for the rest of the experiment at almost 6000 m. Figure 6e shows the clear delay on onset and an underestimation of cloud cover (column-summed cloud fraction) by mesoscale simulations compared to the explicit experiment, missing almost 50% of the domain cloud fraction during the shallow convection period.

c. Cloud and radiative spatial representation

To study the dynamic evolution of clouds and their impact on shortwave radiation, we show in Fig. 7 the time evolution of ice-water content and downward shortwave global radiation profiles for a representative column in each numerical experiment. We show a $9 \times 9 \text{ km}^2$ domain-averaged column for the WRF-LES and NOPAR_3 experiment for an area-equivalent

comparison. The WRF-LES_meso9 experiment shows a growing cloud layer, starting after 1000 UTC, with a rising cloud top that stabilizes at 5000 m after 1300 UTC. The increased density of the cloud from 1300 to 1500 UTC between the 2000- and 4000-m altitude represents the second cloud layer. This increased density reduces the global shortwave radiation at the surface to 400 W m^{-2} (60% of the value above the clouds) at 1400 UTC. The spurious variations of cloud base after 1300 UTC are due to precipitating water that evaporates before reaching the surface.

The figure corroborates the inability of all the mesoscale experiments to reproduce the cloud cycle gradually and as continuum. The NOPAR_9 experiment shows short-lived, sporadic, and relatively shallow but very dense clouds. Their effect in shortwave radiation is much more intense and sudden, to such an extent that the clouds at 1500 UTC prevent almost any shortwave radiation reaching the surface. These very dense clouds are not very frequent in the domain, however, and as a consequence the average surface shortwave radiation is overestimated after 1100 UTC (Fig. 2). The use of a convective parameterization in the mesoscale experiments improves these results. The DENG_9 experiment

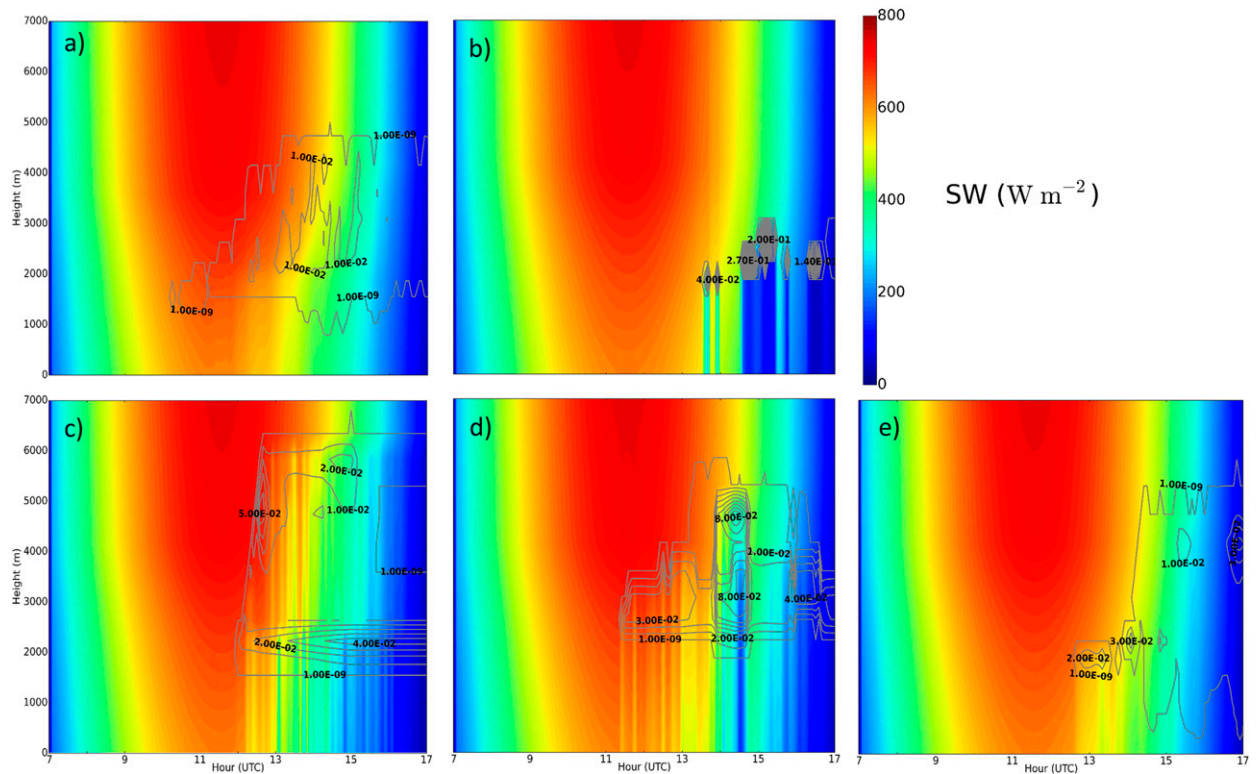


FIG. 7. Time series of vertical profiles of selected representative grid points (or corresponding $9 \times 9 \text{ km}^2$ area) in (a) WRF-LES_meso9, (b) NOPAR_9, (c) DENG_9, (d) GF_9, and (e) NOPAR_3. Global downward shortwave radiation is shown in shaded colors, and ice-liquid water mixing ratio in black contour lines.

shows less sudden and extreme variations in ice-water cloud content as well as on shortwave radiation compared to the NOPAR_9 experiment. However, it shows too high SW until 1200 UTC due to the delay in cloud onset. The presence of the second cloud layer only 30 min after the onset of first clouds conditions the shortwave radiation below 6000 m during the shallow convective period. This fast growth suggests, as stated before, an underestimation of the entrainment in the convective updrafts by the convective scheme. Such a dense second layer (up to 5 g kg^{-1}), combined with a growing low layer, implies a too high variability on the surface shortwave radiation. The continued growth of the low layer after 1430 UTC explains the underestimation of shortwave radiation at the surface of as much as 150 W m^{-2} for this column, a feature also visible on the full domain average in Fig. 2. As shown in Fig. 6 the timing of the first disturbances on SW is better captured by the GF_9 experiment. The rapid growth of the average water content in clouds (up to 8 g kg^{-1} in both layers), in turn, explains an overestimation of SW fluctuations during the shallow convective period similar to that of DENG_9. In this case, the larger extension (Fig. 5) and density (not shown) of the clouds between

1400 and 1500 UTC lead to overestimations of the SW reduction, also found in the domain average (Fig. 2). Finally, we show that a refined horizontal resolution of 3 km improves the shown results without the need of a convective parameterization. Figure 7e shows a delayed onset of clouds and a growth up to 5000 m almost 2 h after the onset of the first cloud, contrasting the immediate onset and growth by DENG_9 in Fig. 7c. Furthermore, values for ice-water cloud content, although overestimated, are closer to the ones suggested by WRF-LES_meso9 of the order of 0.01 g kg^{-1} . Contour lines below 1500 m are due to precipitating water.

Our analysis turns now to study the impact of explicit and parameterized convection in the horizontal distributions. In Figs. 8 and 9 we show the ice-liquid water path over the domain for each experiment, and the instantaneous normalized shortwave radiation along the indicated dashed white lines, with horizontal direct and diffuse components in salmon-orange and yellow, respectively. In addition, the histogram inset in the bottom left corner of each subfigure shows the distribution of ILWP. We selected 1150 UTC as the plotting time given the compromise needed between a developed shallow cumulus field and a minimum impact of previous clouds

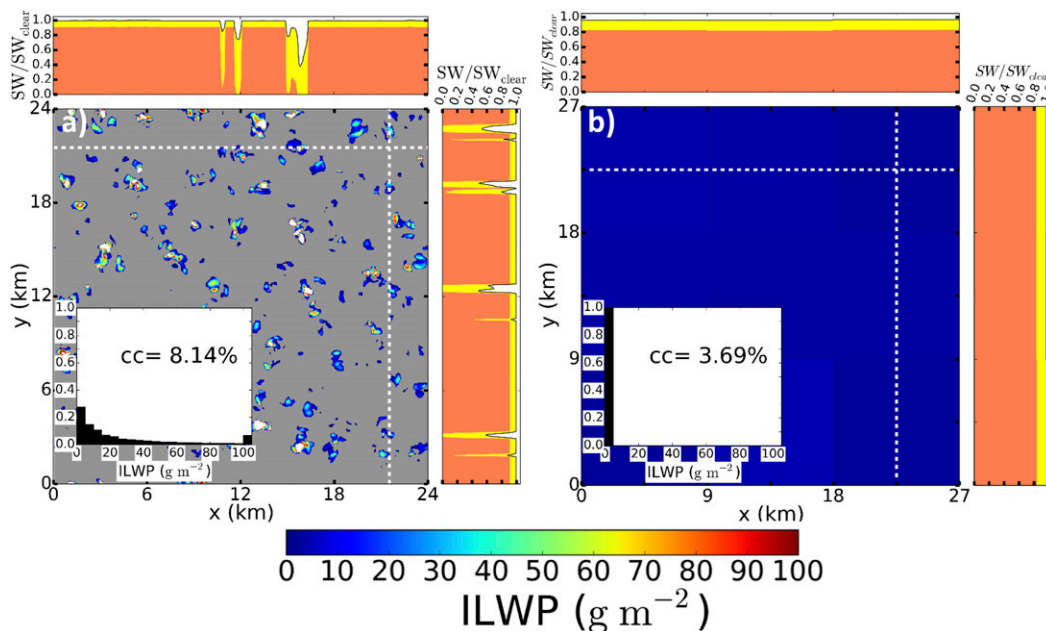


FIG. 8. (a) Instantaneous ILWP for WRF-LES and (b) the WRF-LES_meso9 at 1150 UTC, where columns with ILWP = 0 are displayed in gray. The horizontal and vertical side plots show the global (black line) shortwave radiation at the surface and the contributions of direct (salmon-orange) and diffuse (yellow) shortwave radiation. The inset at the bottom left of each subfigure gives the cloud cover (cc) and ILWP histogram at the shown time. Note that the rightmost bin includes all values above 100 g m^{-2} , including any value above 110 g m^{-2} .

on the experiment thermodynamics. However, we show NOPAR_9 at 1350 UTC as this experiment shows a clear delay in the onset of clouds (Fig. 6e). Figure 8 shows WRF-LES and WRF-LES_meso9 experiments, while the three mesoscale experiments NOPAR_9, DENG_9 and GF_9 are contained in Fig. 9.

The field in the explicit experiment WRF-LES shows a cloud cover of 8.14%, and very high variability of ILWP among different columns with localized maxima of 350 g m^{-2} . The shortwave radiation varies accordingly below the clouds, showing relevant differences in the partition of direct and diffuse SW. Under clouds with low ILWP the global SW reduction is limited, and the contributions of diffuse radiation is larger than that of direct radiation. In contrast, the global SW at the surface is purely diffuse and significantly reduced for denser clouds columns starting at values of ILWP around 10 g m^{-2} . The ILWP histogram shows a gradual decrease toward higher values typical from shallow cumulus fields (Vogelmann et al. 2012). Note that the rightmost bin represents all columns with ILWP above 100 g m^{-2} and that is not negligible as it accounts for nearly 8% of the total. Much of the heterogeneity in ILWP and SW is lost when adapting the results to a coarser mesoscale resolution in WRF-LES_meso9 showed in Fig. 8b. The mesoscale-averaged columns show a much more

homogeneous field with low ILWP values between 0 and 5 g m^{-2} and a 3.69% cloud cover. Similarly, the strong local fluctuations of shortwave radiation, as well as the shift in direct and diffuse partition, are filtered out. The exponential-like decrease for larger ILWP present in the histogram in Fig. 8a shifts to a unique range of ILWP below 5 g m^{-2} .

NOPAR_9 shows too high cloud cover, about 7.35%, with highly heterogeneous values. The global shortwave radiation and its direct and diffuse components vary as in WRF-LES, but at a much larger spatial scale (9 km) and thus overestimating the little spatial variability shown in WRF-LES_meso9. Furthermore, only under much deeper clouds direct radiation disappears. The DENG experiment shows a lower cloud cover to that of WRF-LES_meso9, as also shown in Fig. 6e. Yet we still find too many large ILWP values, as only 40% of the columns contain ILWP within the shallowest $0\text{--}5 \text{ g m}^{-2}$ bin. As a consequence, we find highly varying global SW with too strong minima. The ratio of direct and diffuse radiation does not change much along the domain, with an underestimation of diffuse radiation compared to Fig. 8b. The domain-averaged underestimation is visible in Fig. 2. GF_9 shows an overestimation of the cloud cover compared to WRF-LES_meso9. The spread of ILWP values in GF_9 is further increased,

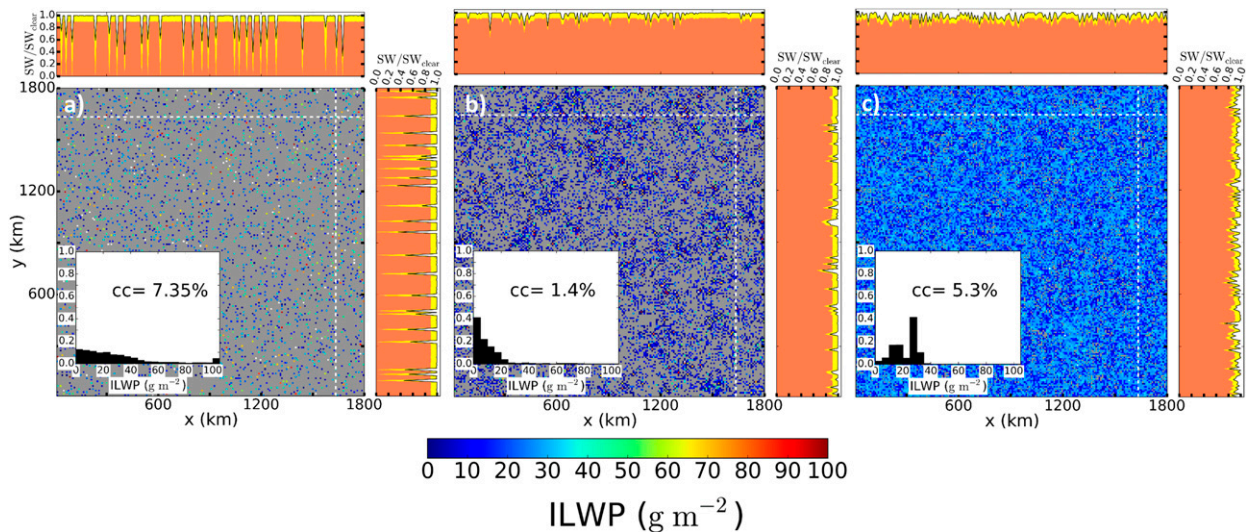


FIG. 9. As in Fig. 8, but for (a) NOPAR_9, (b) DENG_9, and (c) GF_9 experiments at 1150 UTC, except for NOPAR_9 at 1350 UTC.

thus also overestimating the SW reduction due to clouds. GF_9 predicts on average more ice-water content than WRF-LES_meso9 and DENG_9, with more than 90% of the cloudy grid boxes above the expected ILWP range of 0–5 g m^{-2} and a peak at 25–35 g m^{-2} bins. A plausible explanation for this may be the original purpose of the Grell–Freitas parameterization: the deep convection. Thus, the parameterization tends to more frequently generate larger and deeper column clouds than expected from WRF-LES_meso9, as it will be confirmed in Fig. 10.

We show in Fig. 10 the distribution of ice-liquid water paths for our numerical experiments. WRF-LES shows less frequent columns for increasing ILWP, with more columns falling in the most shallow regime (0–10 g m^{-2}) as the experiment evolves (Figs. 10a–c). After removing the resolution effects, we observe most of the clouds to be very shallow (ILWP < 10 g m^{-2}) at 1200 UTC (Fig. 10d), and that starting at 1330 UTC the cloud field stabilizes with most of the clouds falling between the 5 and 30 g m^{-2} bins (Figs. 10e,f).

None of the parameterized experiments are able to represent adequately such an ILWP distribution. NOPAR_9, as first indicated in Fig. 9, shows a delayed cloud cover with too fast growth, and a very wide ILWP spectrum (Figs. 10h,i). DENG_9, although underestimating by a relative 50% the cloud cover at 1200 UTC, shows an acceptable spectra with 60% of the cloudy columns falling within the expected 0–10 g m^{-2} bins. The evolution of the spectra in later hours is, however, very limited and far from the observed in WRF-LES_meso9. In fact, Figs. 10k and 10l suggest a bimodal distribution with maxima in the 0–5 and

35–40 W m^{-2} ranges. As mentioned in Fig. 9, GF_9 experiment shows here its preference for deeper convection. We find GF_9 to overestimate the most common ILWP values by 1200 UTC already and to shift toward deeper values later on. Its bimodal distribution at 1330 and 1500 UTC shows a too rigid preference by this scheme for either shallow convection, with ILWP between 20 and 30 g m^{-2} , and the deeper mode with ILWP ranging from 40 to 60 g m^{-2} . Finally, we find that the horizontal resolution refinement in NOPAR_3 is not enough to obtain a more similar spectra. Indeed, NOPAR_3 still shows too high cloud cover after a delayed onset, and a preference for too shallow clouds, showing that a 3-km horizontal resolution is not enough to account for most of the relevant shallow clouds.

4. Discussion

Lenderink et al. (2004) performed a thorough intercomparison of single column models for a shallow cumulus case, focusing on the turbulence, convection and condensation parameterizations. However, they prescribed both surface fluxes and prescribed radiative tendencies in the atmosphere. Brown et al. (2002) used radiative forcings from another model and prescribed surface fluxes for their turbulence-resolving LES intercomparison on shallow cumulus. Similarly, Siebesma et al. (2003) prescribed surface fluxes for their equilibrium shallow cumulus comparison in LES, and even neglected any cloud radiative effect in the radiation tendencies. In the comparison of explicit precipitating cumulus over sea by van Zanten et al. (2011) a net radiative forcing was prescribed throughout the atmosphere.

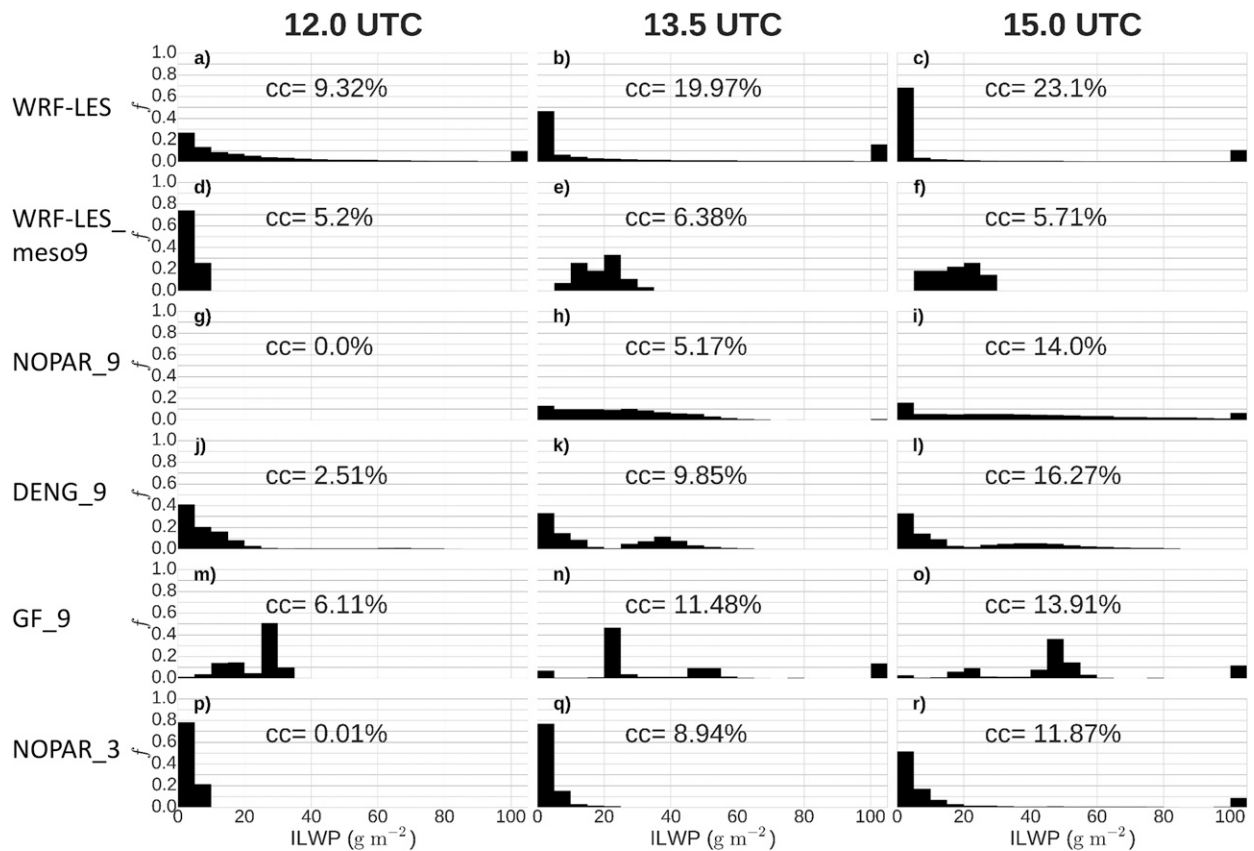


FIG. 10. Cloud cover (cc) and histograms of ice–liquid water path frequency f for (top row) WRF-LES, (second row) WRF-LES_meso9, (third row) NOPAR_9, (fourth row) DENG_9, (fifth row) GF_9, and (bottom row) NOPAR_3 over 15 min interval centered in three selected times during the shallow convection: (left) 1200 UTC, (middle) 1330 UTC, and (right) 1500 UTC.

By omitting the responses of the surface and the radiation to changes in the (parameterized for Lenderink et al. (2004), explicit for the rest) clouds, these studies miss the impact of potential interactions, such as surface dynamic heterogeneities by thick and thin cloud shading or dynamic effects of clouds, and the amplification or dampening of errors induced. Our approach with integrated and interacting cloud, radiation and surface schemes allows for a more realistic and integrated analysis. In fact, the excessive transport of moisture too high in the early phases of the shallow convection time (e.g., see Fig. 4b) impacts the development of the entire simulation by altering the radiation budget and thermodynamic profiles and, consequently, the growth of clouds. In particular, the experiment DENG_9 leads to warm and dry biases within the cloud layer of up to 2 K and more than 1 g kg^{-1} (about 25% of total humidity).

The possibility to solve explicitly the coupling between the radiation perturbations and the surface enables us to demonstrate the inability of the mesoscale experiments to reproduce either the spatial heterogeneities at the surface for global, direct and diffuse

shortwave radiation (Figs. 8 and 9) or the domain-averaged values (Fig. 2). The disagreement lies on an underestimation (overestimation) of diffuse (direct) shortwave radiation at surface by as much as 50% (10%) during most of the shallow convection period. Focused on the radiation effects, Jimenez et al. (2016b) showed that using one of the schemes studied here (Deng et al. 2003) lead to almost no bias for surface SW in the summer months. Our work, considering a more integrated approach, shows that an improvement on average surface SW does not guarantee a realistic representation of the boundary layer and cloud processes, raising the possibility of mutually canceling errors or compensating effects.

The need by convective parameterizations to account for shallow convection in ever-refining resolution has been mentioned as one of the main challenges among the numerical weather prediction models (Hong and Dudhia 2012). Thus, the spatial characterization, and the sensitivity of current regional models to horizontal resolution is explored in our study in section 3c. As already pointed out in previous studies (Dudhia 2014), the

biases due to the convective parameterizations used in our study affect the thermodynamical state of the atmosphere and condition the further development of the experiments. This is improved when using no parameterization (NOPAR), at the expense of having a clearly nonrealistic cloud cover (Fig. 6) and characteristics (Fig. 10). Refining the horizontal resolution to 3 km without convective scheme improves the representation for cloud fraction (Fig. 5) and cloud cover development (Fig. 7e), partly due to better mixing within the subcloud layer. Yet the average ILWP (Fig. 1) as well as its distribution (Fig. 10) shows large discrepancies with respect to a fully explicit LES experiment, by underestimating the presence of deeper clouds. In consequence, our study indicates that parameterizations are still needed for shallow convection as long as horizontal resolutions do not reach below 3 km.

Finally, the results shown in this study are not only relevant for the regional numerical weather forecasting community, as the use of such a coupled model provides interesting outcome to several communities. In fact, the errors in shortwave radiation at the surface and, particularly, the misrepresentation of direct and diffuse radiation ratios by convective parameterizations, as well as their different spatial distributions are of critical relevance for solar energy forecast (Pedro and Coimbra 2012). Direct and diffuse radiation partition is also of importance for the growing number of land surface models sensitive to it, such as the DALES model used here or the land surface model used by the Integrated Forecasting System by ECMWF (Boussetta et al. 2013). An adequate representation of direct and diffuse ratios is also necessary for accurate estimations on gross primary productivity by land surface models at all time scales (Alton et al. 2007; Cheng et al. 2015), and CO₂ concentration and carbon cycle estimations (Mercado et al. 2009). In particular, the presence of diffuse radiation under certain conditions has been broadly linked to increased vegetation activity (Kanniah et al. 2012). Likewise, modeled isoprene biogenic emissions, known to be sensitive to direct/diffuse ratios (Guenther 2013; Laffineur et al. 2013), may benefit from a more realistic representation such as the one shown in our explicit numerical experiments. This is also applicable to calculations of other chemical compound estimations (Madronich 1987).

5. Conclusions

Our research presents an integrated study on the effects exerted on cloud and boundary layer dynamics, radiation and surface by the performance of shallow

convection parameterizations. Our novel methodology with coupled schemes allows us to analyze the effects of convective parameterizations on the thermodynamics, radiation and surface of the simulation, as opposed to previous studies with prescribed surface or radiative fluxes. By keeping two different explicit LES model simulations (DALES and WRF-LES) as reference, we examine how convective schemes in WRF-Solar represent an idealized midlatitude shallow convective summer day. We perform three simulations at the typical mesoscale operational resolution (i.e., 9 km in horizontal and 50 vertical levels up to 20 km): with no parameterized convection, and with two convective parameterizations by Deng et al. (2014) and Grell and Freitas (2014), respectively. An extra experiment at an intermediate horizontal resolution of 3 km is carried out without any convective scheme to explore the convection representation within the gray zone. Coinciding vertical profiles of state variables and fluxes, time evolution and spatial distributions of clouds by both LES ensure the robustness of the case.

We here summarize the findings, based on one representative but idealized case of shallow cumulus over the Netherlands, addressing different fields of interest:

- Interesting for land surface model and solar energy harvesting, the domain-averaged global horizontal irradiance at the surface is improved when using the convective parameterizations. However, the spatial (horizontal and vertical) variability and the direct and diffuse partition are not properly represented: they show too much variability and too little (much) diffuse (direct) radiation. See Figs. 2, 7, 8, and 9.
- Related to the atmosphere thermodynamic structure, the parameterizations worsen the temperature and moisture profiles within the mixed boundary layer and cloud layer above: the cooling is too small in the cloud layer; there is too much drying, and too much moisture transported too high. See Figs. 3 and 4.
- On cloud characteristics, the timing of onset is improved by parameterizations. However, they predict too high cloud bases, too dense clouds and a too early and sudden creation of a too high second cloud layer. There is too much horizontal variability within the domain: The parameterizations tend to describe a cloud field with too deep clouds and with a too large domain-averaged cloud cover. See Figs. 1, 5, 6, 9, and 10.

The results of our study show that state of the art parameterizations for shallow convection are still not able to reproduce the essential characteristics that clouds exert on the surface-atmosphere system. Although they may predict variables such as domain-averaged shortwave

radiation correctly, a broader analysis is needed to assess whether the schemes show the right values for the right reasons. Intermediate horizontal resolutions of 3 km proved to be not enough to reproduce the cloud features and effects by the fully explicit LES, as the smallest yet relevant scales of the shallow convection are not explicitly resolved.

Acknowledgments. The first author would like to acknowledge the economic support by RAL and MMM departments for the stay at NCAR. This study was supported by the grant from the NWO ALW Open Programme (824.15.013). Computing resources (ark:/85065/d7wd3xhc) were provided by the Climate Simulation Laboratory at NCAR's Computational and Information Systems Laboratory, sponsored by the National Science Foundation and other agencies. The authors would like to acknowledge the helpful comments by anonymous reviewers during the review process.

REFERENCES

- Alton, P., P. North, and S. Los, 2007: The impact of diffuse sunlight on canopy light-use efficiency, gross photosynthetic product and net ecosystem exchange in three forest biomes. *Global Change Biol.*, **13**, 776–787, <https://doi.org/10.1111/j.1365-2486.2007.01316.x>.
- Arakawa, A., 2004: The cumulus parameterization problem: Past, present, and future. *J. Climate*, **17**, 2493–2525, [https://doi.org/10.1175/1520-0442\(2004\)017<2493:RATCPP>2.0.CO;2](https://doi.org/10.1175/1520-0442(2004)017<2493:RATCPP>2.0.CO;2).
- , J.-H. Jung, and C.-M. Wu, 2011: Toward unification of the multiscale modeling of the atmosphere. *Atmos. Chem. Phys.*, **11**, 3731–3742, <https://doi.org/10.5194/acp-11-3731-2011>.
- Boussetta, S., and Coauthors, 2013: Natural land carbon dioxide exchanges in the ECMWF Integrated Forecasting System: Implementation and offline validation. *J. Geophys. Res. Atmos.*, **118**, 5923–5946, <https://doi.org/10.1002/jgrd.50488>.
- Brown, A. R., and Coauthors, 2002: Large-eddy simulation of the diurnal cycle of shallow cumulus convection over land. *Quart. J. Roy. Meteor. Soc.*, **128**, 1075–1093, <https://doi.org/10.1256/003590002320373210>.
- Casso-Torralba, P., J. Vilà-Guerau de Arellano, F. Bosveld, M. R. Soler, A. Vermeulen, C. Werner, and E. Moors, 2008: Diurnal and vertical variability of the sensible heat and carbon dioxide budgets in the atmospheric surface layer. *J. Geophys. Res.*, **113**, D12119, <https://doi.org/10.1029/2007JD009583>.
- Cheng, S. J., G. Bohrer, A. L. Steiner, D. Y. Hollinger, A. Suyker, R. P. Phillips, and K. J. Nadelhoffer, 2015: Variations in the influence of diffuse light on gross primary productivity in temperate ecosystems. *Agric. For. Meteorol.*, **201**, 98–110, <https://doi.org/10.1016/j.agrformet.2014.11.002>.
- Ching, J., R. Rotunno, M. LeMone, A. Martilli, B. Kosovic, P. A. Jimenez, and J. Dudhia, 2014: Convectively induced secondary circulations in fine-grid mesoscale numerical weather prediction models. *Mon. Wea. Rev.*, **142**, 3284–3302, <https://doi.org/10.1175/MWR-D-13-00318.1>.
- Couvreur, F., and Coauthors, 2015: Representation of daytime moist convection over the semi-arid tropics by parametrizations used in climate and meteorological models. *Quart. J. Roy. Meteor. Soc.*, **141**, 2220–2236, <https://doi.org/10.1002/qj.2517>.
- Deng, A., N. L. Seaman, and J. S. Kain, 2003: A shallow-convection parameterization for mesoscale models. Part I: Submodel description and preliminary applications. *J. Atmos. Sci.*, **60**, 34–56, [https://doi.org/10.1175/1520-0469\(2003\)060<0034:ASCPFM>2.0.CO;2](https://doi.org/10.1175/1520-0469(2003)060<0034:ASCPFM>2.0.CO;2).
- , B. Gaudet, J. Dudhia, and K. Alapaty, 2014: Implementation and evaluation of a new shallow convection scheme in WRF. *26th Conf. on Weather Analysis and Forecasting/22nd Conf. on Numerical Weather Prediction*, Atlanta, GA, Amer. Meteor. Soc., 12.5, <https://ams.confex.com/ams/94Annual/webprogram/Paper236925.html>.
- Dudhia, J., 2014: A history of mesoscale model development. *Asia-Pac. J. Atmos. Sci.*, **50**, 121–131, <https://doi.org/10.1007/s13143-014-0031-8>.
- Fowler, L. D., W. C. Skamarock, G. A. Grell, S. R. Freitas, and M. G. Duda, 2016: Analyzing the Grell–Freitas convection scheme from hydrostatic to nonhydrostatic scales within a global model. *Mon. Wea. Rev.*, **144**, 2285–2306, <https://doi.org/10.1175/MWR-D-15-0311.1>.
- Freitas, S. R., and Coauthors, 2017: The Brazilian developments on the Regional Atmospheric Modeling System (BRAMS 5.2): An integrated environmental model tuned for tropical areas. *Geosci. Model Dev.*, **10**, 189–222, <https://doi.org/10.5194/gmd-10-189-2017>.
- Grabowski, W. W., 2014: Extracting microphysical impacts in large-eddy simulations of shallow convection. *J. Atmos. Sci.*, **71**, 4493–4499, <https://doi.org/10.1175/JAS-D-14-0231.1>.
- Grell, G. A., 1993: Prognostic evaluation of assumptions used by cumulus parameterizations. *Mon. Wea. Rev.*, **121**, 764–787, [https://doi.org/10.1175/1520-0493\(1993\)121<0764:PEOAUB>2.0.CO;2](https://doi.org/10.1175/1520-0493(1993)121<0764:PEOAUB>2.0.CO;2).
- , and D. Devenyi, 2002: A generalized approach to parameterizing convection combining ensemble and data assimilation techniques. *Geophys. Res. Lett.*, **29**, 1693, <https://doi.org/10.1029/2002GL015311>.
- , and S. R. Freitas, 2014: A scale and aerosol aware stochastic convective parameterization for weather and air quality modeling. *Atmos. Chem. Phys.*, **14**, 5233–5250, <https://doi.org/10.5194/acp-14-5233-2014>.
- Gronemeier, T., F. Kanani-Sühring, and S. Raasch, 2016: Do shallow cumulus clouds have the potential to trigger secondary circulations via shading? *Bound.-Layer Meteorol.*, **162**, 143–169, <https://doi.org/10.1007/s10546-016-0180-7>.
- Guenther, A., 2013: Upscaling biogenic volatile compound emissions from leaves to landscapes. *Biology, Controls and Models of Tree Volatile Organic Compound Emissions*, Ü. Niinemets and R. Monson, Eds., Springer, 391–414, https://doi.org/10.1007/978-94-007-6606-8_14.
- Guichard, F., and Coauthors, 2004: Modelling the diurnal cycle of deep precipitating convection over land with cloud-resolving models and single-column models. *Quart. J. Roy. Meteor. Soc.*, **130**, 3139–3172, <https://doi.org/10.1256/qj.03.145>.
- Heus, T., and Coauthors, 2010: Formulation of the Dutch Atmospheric Large-Eddy Simulation (DALES) and overview of its applications. *Geosci. Model Dev.*, **3**, 415–444, <https://doi.org/10.5194/gmd-3-415-2010>.
- Hong, S.-Y., and J. Dudhia, 2012: Next-generation numerical weather prediction: Bridging parameterization, explicit clouds, and large eddies. *Bull. Amer. Meteor. Soc.*, **93**, ES6–ES9, <https://doi.org/10.1175/2011BAMS3224.1>.

- , H.-M. H. Juang, and Q. Zhao, 1998: Implementation of prognostic cloud scheme for a regional spectral model. *Mon. Wea. Rev.*, **126**, 2621–2639, [https://doi.org/10.1175/1520-0493\(1998\)126<2621:IOPCSF>2.0.CO;2](https://doi.org/10.1175/1520-0493(1998)126<2621:IOPCSF>2.0.CO;2).
- Horn, G. L., H. G. Ouwersloot, J. Vilà-Guerau de Arellano, and M. Sikma, 2015: Cloud shading effects on characteristic boundary-layer length scales. *Bound.-Layer Meteor.*, **157**, 237–263, <https://doi.org/10.1007/s10546-015-0054-4>.
- Iacono, M. J., J. S. Delamere, E. J. Mlawer, M. W. Shephard, S. A. Clough, and W. D. Collins, 2008: Radiative forcing by long-lived greenhouse gases: Calculations with the AER radiative transfer models. *J. Geophys. Res.*, **113**, D13103, <https://doi.org/10.1029/2008JD009944>.
- Jacobs, C. M. J., and H. A. R. de Bruin, 1997: Predicting regional transpiration at elevated atmospheric CO₂: Influence of the PBL–vegetation interaction. *J. Appl. Meteor.*, **36**, 1663–1675, [https://doi.org/10.1175/1520-0450\(1997\)036<1663:PRTAEA>2.0.CO;2](https://doi.org/10.1175/1520-0450(1997)036<1663:PRTAEA>2.0.CO;2).
- Jakub, F., and B. Mayer, 2017: The role of 1-D and 3-D radiative heating in the organization of shallow cumulus convection and the formation of cloud streets. *Atmos. Chem. Phys.*, **17**, 13 317–13 327, <https://doi.org/10.5194/acp-17-13317-2017>.
- Jimenez, P. A., S. Alessandrini, S. E. Haupt, A. Deng, B. Kosovic, J. A. Lee, and L. D. Monache, 2016a: The role of unresolved clouds on short-range global horizontal irradiance predictability. *Mon. Wea. Rev.*, **144**, 3099–3107, <https://doi.org/10.1175/MWR-D-16-0104.1>.
- , and Coauthors, 2016b: WRF-Solar: Description and clear-sky assessment of an augmented NWP model for solar power prediction. *Bull. Amer. Meteor. Soc.*, **97**, 1249–1264, <https://doi.org/10.1175/BAMS-D-14-00279.1>.
- Kain, J. S., and J. M. Fritsch, 1990: A one-dimensional entraining/detraining plume model and its application in convective parameterization. *J. Atmos. Sci.*, **47**, 2784–2802, [https://doi.org/10.1175/1520-0469\(1990\)047<2784:AODEPM>2.0.CO;2](https://doi.org/10.1175/1520-0469(1990)047<2784:AODEPM>2.0.CO;2).
- Kanniah, K. D., J. Beringer, P. North, and L. Hutley, 2012: Control of atmospheric particles on diffuse radiation and terrestrial plant productivity: A review. *Prog. Phys. Geogr.*, **36**, 209–237, <https://doi.org/10.1177/0309133311434244>.
- Klinger, C., B. Mayer, F. Jakub, T. Zinner, S.-B. Park, and P. Gentile, 2017: Effects of 3-D thermal radiation on the development of a shallow cumulus cloud field. *Atmos. Chem. Phys.*, **17**, 5477–5500, <https://doi.org/10.5194/acp-17-5477-2017>.
- Laffineur, Q., M. Aubinet, N. Schoon, C. Amelynck, J.-F. Müller, J. Dewulf, K. Steppe, and B. Heinesch, 2013: Impact of diffuse light on isoprene and monoterpene emissions from a mixed temperate forest. *Atmos. Environ.*, **74**, 385–392, <https://doi.org/10.1016/j.atmosenv.2013.04.025>.
- Lenderink, G., and Coauthors, 2004: The diurnal cycle of shallow cumulus clouds over land: A single-column model intercomparison study. *Quart. J. Roy. Meteor. Soc.*, **130**, 3339–3364, <https://doi.org/10.1256/qj.03.122>.
- Liou, K.-N., 2002: *An Introduction to Atmospheric Radiation*. 2nd ed. International Geophysics Series, Vol. 84, Academic Press, 583 pp.
- Madronich, S., 1987: Photodissociation in the atmosphere: 1. Actinic flux and the effects of ground reflections and clouds. *J. Geophys. Res.*, **92**, 9740–9752, <https://doi.org/10.1029/JD092iD08p09740>.
- Mercado, L. M., N. Bellouin, S. Sitch, O. Boucher, C. Huntingford, M. Wild, and P. M. Cox, 2009: Impact of changes in diffuse radiation on the global land carbon sink. *Nature*, **458**, 1014–1017, <https://doi.org/10.1038/nature07949>.
- Nakanishi, M., and H. Niino, 2006: An improved Mellor–Yamada Level-3 Model: Its numerical stability and application to a regional prediction of advection fog. *Bound.-Layer Meteor.*, **119**, 397–407, <https://doi.org/10.1007/s10546-005-9030-8>.
- Nieuwstadt, F. T. M., and R. A. Brost, 1986: The decay of convective turbulence. *J. Atmos. Sci.*, **43**, 532–546, [https://doi.org/10.1175/1520-0469\(1986\)043<0532:TDOCT>2.0.CO;2](https://doi.org/10.1175/1520-0469(1986)043<0532:TDOCT>2.0.CO;2).
- Niu, G., and Coauthors, 2011: The community Noah land surface model with multiparameterization options (Noah-MP): 1. Model description and evaluation with local scale measurements. *J. Geophys. Res.*, **116**, D12109, <https://doi.org/10.1029/2010JD015139>.
- Ouwersloot, H. G., A. F. Moene, J. J. Attema, and J. V.-G. de Arellano, 2017: Large-eddy simulation comparison of neutral flow over a canopy: Sensitivities to physical and numerical conditions, and similarity to other representations. *Bound.-Layer Meteor.*, **162**, 71–89, <https://doi.org/10.1007/s10546-016-0182-5>.
- Pedro, H. T., and C. F. Coimbra, 2012: Assessment of forecasting techniques for solar power production with no exogenous inputs. *Sol. Energy*, **86**, 2017–2028, <https://doi.org/10.1016/j.solener.2012.04.004>.
- Pedruzo-Bagazgoitia, X., H. G. Ouwersloot, M. Sikma, C. C. van Heerwaarden, C. M. J. Jacobs, and J. Vilà-Guerau de Arellano, 2017: Direct and diffuse radiation in the shallow cumulus–vegetation system: Enhanced and decreased evapotranspiration regimes. *J. Hydrometeorol.*, **18**, 1731–1748, <https://doi.org/10.1175/JHM-D-16-0279.1>.
- Schalkwijk, J., H. J. Jonker, A. P. Siebesma, and F. C. Bosveld, 2015: A year-long large-eddy simulation of the weather over Cabauw: An overview. *Mon. Wea. Rev.*, **143**, 828–844, <https://doi.org/10.1175/MWR-D-14-00293.1>.
- Siebesma, A. P., and Coauthors, 2003: A large eddy simulation intercomparison study of shallow cumulus convection. *J. Atmos. Sci.*, **60**, 1201–1219, [https://doi.org/10.1175/1520-0469\(2003\)60<1201:ALESIS>2.0.CO;2](https://doi.org/10.1175/1520-0469(2003)60<1201:ALESIS>2.0.CO;2).
- Sikma, M., and J. Vilà-Guerau de Arellano, 2019: Substantial reductions in cloud cover and moisture transport by dynamic plant responses. *Geophys. Res. Lett.*, **46**, 1870–1878, <https://doi.org/10.1029/2018GL081236>.
- , H. Ouwersloot, X. Pedruzo-Bagazgoitia, C. van Heerwaarden, and J. V.-G. de Arellano, 2018: Interactions between vegetation, atmospheric turbulence and clouds under a wide range of background wind conditions. *Agric. For. Meteorol.*, **255**, 31–43, <https://doi.org/10.1016/j.agrformet.2017.07.001>.
- Skamarock, W. C., and Coauthors, 2008: A description of the Advanced Research WRF version 3. NCAR Tech. Note NCAR/TN-475+STR, 113 pp., <https://doi.org/10.5065/D68S4MVH>.
- Smagorinsky, J., 1963: General circulation experiments with the primitive equations. *Mon. Wea. Rev.*, **91**, 99–164, [https://doi.org/10.1175/1520-0493\(1963\)091<0099:GCEWTP>2.3.CO;2](https://doi.org/10.1175/1520-0493(1963)091<0099:GCEWTP>2.3.CO;2).
- Thompson, G., P. R. Field, R. M. Rasmussen, and W. D. Hall, 2008: Explicit forecasts of winter precipitation using an improved bulk microphysics scheme. Part II: Implementation of a new snow parameterization. *Mon. Wea. Rev.*, **136**, 5095–5115, <https://doi.org/10.1175/2008MWR2387.1>.
- Trenberth, K. E., J. T. Fasullo, and J. Kiehl, 2009: Earth's global energy budget. *Bull. Amer. Meteor. Soc.*, **90**, 311–324, <https://doi.org/10.1175/2008BAMS2634.1>.
- van Heerwaarden, C. C., J. Vilà-Guerau de Arellano, A. Gounou, F. Guichard, and F. Couvreux, 2010: Understanding the daily cycle of evapotranspiration: A method to quantify the

- influence of forcings and feedbacks. *J. Hydrometeor.*, **11**, 1405–1422, <https://doi.org/10.1175/2010JHM1272.1>.
- van Zanten, M. C., and Coauthors, 2011: Controls on precipitation and cloudiness in simulations of trade-wind cumulus as observed during RICO. *J. Adv. Model. Earth Syst.*, **3**, M06001, <https://doi.org/10.1029/2011MS000056>.
- Vilà-Guerau de Arellano, J., H. G. Ouwersloot, D. Baldocchi, and C. M. J. Jacobs, 2014: Shallow cumulus rooted in photosynthesis. *Geophys. Res. Lett.*, **41**, 1796–1802, <https://doi.org/10.1002/2014GL059279>.
- Vogelmann, A. M., and Coauthors, 2012: RACORO extended-term aircraft observations of boundary layer clouds. *Bull. Amer. Meteor. Soc.*, **93**, 861–878, <https://doi.org/10.1175/BAMS-D-11-00189.1>.
- Wyngaard, J. C., 2004: Toward numerical modeling in the “Terra Incognita”. *J. Atmos. Sci.*, **61**, 1816–1826, [https://doi.org/10.1175/1520-0469\(2004\)061<1816:TNMITT>2.0.CO;2](https://doi.org/10.1175/1520-0469(2004)061<1816:TNMITT>2.0.CO;2).
- Xu, K.-M., and D. A. Randall, 1996: A semiempirical cloudiness parameterization for use in climate models. *J. Atmos. Sci.*, **53**, 3084–3102, [https://doi.org/10.1175/1520-0469\(1996\)053<3084:ASCPFU>2.0.CO;2](https://doi.org/10.1175/1520-0469(1996)053<3084:ASCPFU>2.0.CO;2).